Journal of Alloys and Compounds 868 (2021) 159201

Contents lists available at ScienceDirect

Journal of Alloys and Compounds

journal homepage: www.elsevier.com/locate/jalcom

New stable two dimensional silicon carbide nanosheets

Qun Wei[a], Ying Yang[b,c], Guang Yang[b,d], Xihong Peng[b,*]

[a] School of Physics and Optoelectronic Engineering, Xidian University, Xi'an, Shaanxi 710071, PR China
[b] College of Integrative Sciences and Arts, Arizona State University, Mesa, Arizona 85212, USA
[c] School of Automation and Information Engineering, Xi'an University of Technology, Xi'an, Shaanxi 710048, PR China
[d] School of Science, Hebei University of Science and Technology, Shijiazhuang, Hebei 050018, PR China

ARTICLE INFO

Article history:
Received 13 December 2020
Received in revised form 10 February 2021
Accepted 13 February 2021
Available online 17 February 2021

Keywords:
2D silicon carbide
Strain-stress relation
Moduli
Band structure
Band gap
Hydrogenation
Strain engineering

ABSTRACT

We predict the existence of new two dimensional (2D) silicon carbide nanostructures employing ab initio density-functional theory calculations. These structures are composed of tetragonal and hexagonal rings with C—C and Si—C bonds arranged in a buckling plane. They are proven to be thermodynamically and mechanically stable with relatively low formation energy, implying potential fabrication in labs. They exhibit strong ductility and anisotropicity from their strain-stress relations and directional dependence of mechanical moduli. The materials maintain phonon stability upon the application of mechanical strain up to 27% with fantastic ductile property. The proposed 2D SiC_2 structure possesses a tiny direct band gap of 0.02 eV predicted using HSE06 functional and the band gap can be opened up through multiple approaches such as hydrogenation and strain application. The gap values can be strategically tuned in the range of 0.02–1.72 eV and the direct/indirect gap nature can be further manipulated. In contrast, a closely related isostructural 2D SiC shows an indirect HSE band gap of 1.80 eV and strain engineering its value between 0.0–1.95 eV. The unique properties in these newly proposed structures might have potential applications in future nanomechanics and electronics.

1. Introduction

Successful fabrication of two dimensional (2D) materials such as group IV graphene [1–3] and silicene [4–6] prompt incredible interests in 2D materials research. Graphene was explored enormously in practical applications [1–3]. Silicene embracing graphene-like crystal lattice with a low-buckled geometry was also been extensively studied [4–6] due to its compatibility and desirability in device applications [6]. However, both graphene and silicene are semimetals with π and π* states touching each other at the Fermi level [7]. The zero band gap in graphene and silicene limits their widespread applications in optoelectronic devices such as light-emitting diodes, field effect transistors, and solar cells. Numerous strategies have been investigated to open the band gap in graphene and silicene, including substrate effects [4–6], nanoribbons with quantum confinement [8,9], alloys [10], applying external electric fields [11], hydrogenation [12], chemical functionalization [13], doping [14], introducing defects [15] and applying mechanical strain [16]. Another way to engineer desirable band gap is to explore other 2D materials. In addition to graphene (silicene), various other 2D carbon (silicon) allotropes, such as penta-graphene [17], T-graphene [18], S-graphene [19], α-, β-, δ-graphynes [20,21], tetrahex-carbon [22] were further studied and the properties of each unique structure were reported in literature.

For silicon-carbon binary compounds, silicon carbide is known to have more than 250 crystalline polytypisms including cubic SiC, 4 H- and 6 H-SiC. Silicon carbide compounds traditionally have four-coordinated tetragonal building blocks with remarkable electronic properties and superior thermal, chemical, and mechanical stability. Electronic devices based upon these properties have been utilized at temperatures in excess of 300 °C and in harsh environments. Recently, numerous 2D silicon carbide compounds were also fabricated and proposed, for instance, experimentally synthesized graphitic SiC [4–6], planar SiC_2 silagraphene with tetra-coordinated Si [23], planar graphitic SiC_2 [24], carbon-rich SiC_3 [25], g-SiC_2 [24], pt-SiC_2 [23], SiC_6-SW [26], SiC_2-b [26], SiC_2-p [26], quasi-planar tetragonal SiC and SiC_2 [27], penta-SiC_2 [28], a series of silagraphyne [27], silicon-rich Si_3C [26], and recently reported tetrahex SiC [29]. These 2D nanostructures exhibit either metallic (semimetal) or semiconducting behavior with a finite band gap.

In this work, we propose a new type of 2D silicon carbide nanosheet with a buckled geometry. Similar to the structure of

* Corresponding author.
E-mail address: xihong.peng@asu.edu (X. Peng).

https://doi.org/10.1016/j.jallcom.2021.159201
0925-8388/

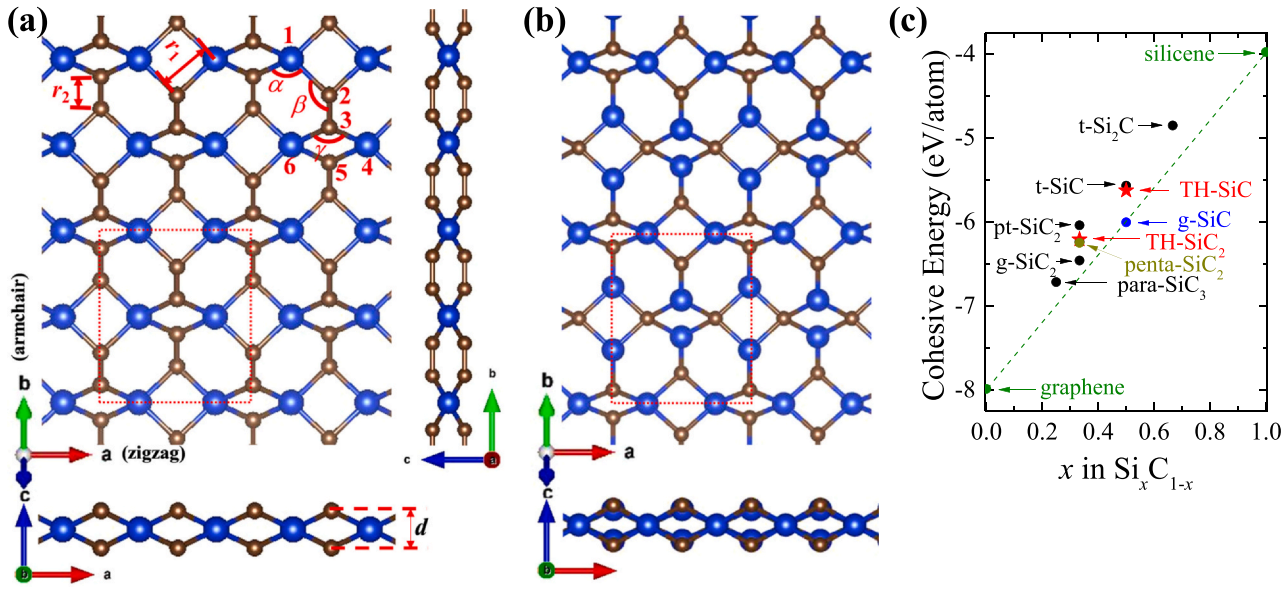

Fig. 1. Snapshots of the 2D (a) TH-SiC_2 and (b) TH-SiC structures viewed from various orientations. Si and C atoms are in blue and brown, respectively. The buckling thickness is labeled as d. The bond lengths, bond angles are denoted. The dashed rectangles represent a conventional cell containing 12 atoms. (c) Cohesive energy of some 2D Si_xC_{1-x} compounds. The green dashed line connecting the energies of graphene and silicene is a guide for eye. For structural details, one can refer to pertinent papers (para SiC_3 [25], penta-SiC_2 [28], g-SiC [42], g-SiC_2 [24], pt-SiC_2 [23], t-SiC [27], t-Si_2C [27]) (For interpretation of the references to colour in this figure legend, the reader is referred to the web version of this article.).

tetrahex-carbon [22], the new 2D silicon carbide network contains tetragonal (T) and hexagonal (H) rings, named as TH-SiC_2 and TH-SiC. In TH-SiC_2, the four-coordinated (sp^3) Si atoms are sandwiched between two sublayers of three-coordinated (sp^2) carbon atoms. In TH-SiC, both Si and C atoms can be sp^3 or sp^2 hybridized. Through the calculations of first-principles density-functional theory (DFT) [30], these new nanostructures are proven to be thermodynamically and mechanically stable. They have relatively low formation energy and indicate potential fabrication in labs. In the frame work of DFT, we find that TH-SiC_2 possesses a tiny band gap of 0.02 eV predicted by the hybrid Heyd-Scuseria-Ernzerhof (HSE)06 method [31,32], while TH-SiC has a finite indirect band gap of 1.80 eV. These materials are ductile to sustain a high strain up to 27% while still maintaining phonon stability. Their band gap can be effectively manipulated through various strategies including hydrogenation and mechanical strain application.

2. Computational details

The first-principles DFT [30] calculations were carried out using the VASP package [33,34] with projector-augmented wave (PAW) potentials [35,36]. Perdew-Burke-Ernzerhof (PBE) exchange-correlation functional [37] is selected for the geometry relaxation. The hybrid (HSE)06 method [31,32] is used to calculate electronic band structures and band gaps due to its improved accuracy on predicting semiconductor band gaps.

The wave functions of valence electrons are described using a plane wave basis set with a kinetic energy cutoff 900 eV. The reciprocal space is meshed 15 × 13 × 1 by using the Monkhorst-Pack method [38]. A conjugate-gradient algorithm [39] is used to relax the ions into their instantaneous ground state. The energy convergence criterion for electronic self-consistent procedure is set to be 10^{-8} eV and the force is converged to be less than 10^{-4} eV/Å for geometry optimization of the simulation cell. The kinetic energy cutoff 500 eV for the plane wave basis set is utilized for the HSE band structure calculations. A total of 11 *k*-points are collected along each high symmetry line in the reciprocal space for the band structure calculations. The **c**-vector of the unit cell is set to be 20 Å to ensure sufficient vacuum space (>16 Å) included in the calculations to minimize the interaction between the system and its replicas resulted from periodic boundary conditions. Phonon spectrum is conducted by density functional perturbation theory method using a supercell approach in the PHONOPY code [40] with the forces computed from VASP [33,34]. Structural snapshots and electron orbital contour plots are generated using VESTA program [41].

3. Results and discussion

3.1. Structure and thermodynamic stability

Fig. 1(a) and (b) present the crystal structures of the newly predicted 2D TH-SiC_2 and its related TH-SiC. They are buckled three-

Table 1
Summary of structural parameters and basic properties of TH-SiC_2, TH-SiC, penta-SiC_2, tetrahex-C, penta-graphene, graphene, and silicene. Lattice constants a, b, buckling thickness d, and bond lengths r_1, r_2 are in unit of Å, cohesive E_{coh} and formation energies E_{form} are in eV/atom, HSE predicted band gap E_g in eV. The formation energy is calculated using graphene and silicene as references (thus *zero for graphene and silicene). Reference: TH-SiC [29], penta-SiC_2 [28], tetrahex-C [22,43], penta-graphene [17], silicene [7,27].

Structures	*a*	*b*	*d*	r_1	r_2	E_{coh}	E_{form}	E_g	Gap nature
TH-SiC_2	5.52	7.20	1.34	1.90	1.35	-6.21	0.44	0.02	Direct
TH-SiC	5.53	7.63	1.60	1.88	1.72	-5.63	0.61	1.80	Indirect
Penta-SiC2	4.41	4.41	1.33	1.91	1.36	-6.25	0.40	2.85	Indirect
Tetrahex-C	4.53	6.10	1.16	1.53	1.34	-7.12	0.87	2.64	Direct
Penta-graphene	3.64	3.64	1.20	1.55	1.34	-7.09	0.91	3.25	Indirect
Graphene	2.46	2.46	0.00	1.42	1.42	-7.99	0*	0.00	Semimetal
Silicene	3.87	3.87	0.44	2.28	2.28	-3.98	0*	0.00	Semimetal

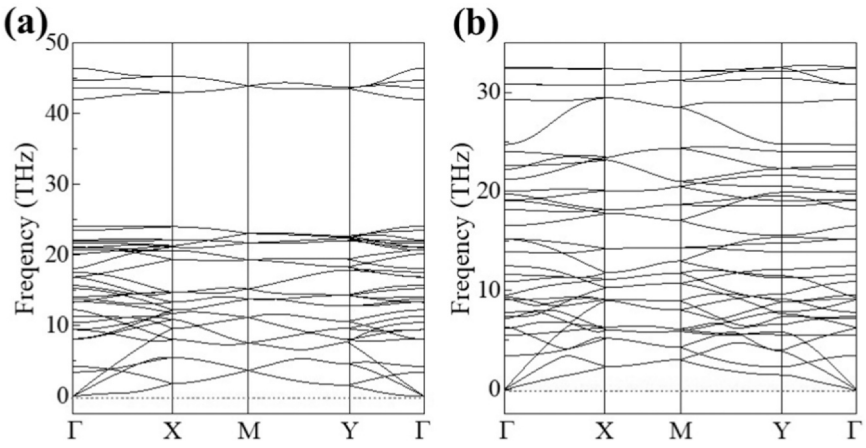

Fig. 2. Phonon spectra of the 2D (a) TH-SiC_2 and (b) TH-SiC nanosheets.

sublayer crystal structures with four-coordinated (sp^3) atoms being sandwiched between two sublayers of three-coordinated (sp^2) atoms. The rectangular conventional cell contains 12 atoms, 4 Si and 8 C atoms in TH-SiC_2 and 6 Si and 6 C in TH-SiC. The buckling thickness d describes the distance between the top and bottom sublayers of the sp^2-atoms. The length r_1 is the Si—C bond in the tetragonal rings and r_2 is the C—C bond (Si—C bond) in the hexagonal rings for the TH-SiC_2 (TH-SiC) structure.

The relaxed lattice constants for the 2D TH-SiC_2 are a = 5.52 Å and b = 7.20 Å. The buckling thickness d is 1.34 Å. The bond lengths r_1 and r_2 are predicted to be 1.90 Å and 1.35 Å, respectively. The calculated bond angles denoted in Fig. 1(a) are $\alpha = 107.5°$, $\beta = 126.3°$, and $\gamma = 92.9°$. It is clear from the tilted-axis view in Fig. 1(a), two neighbored hexagonal rings along the **a**-axis (i.e. x-axis or the zigzag direction) are not coplanar. The dihedral angle between these two hexagonal rings is denoted as ϕ_{1234} by the neighboring atoms 1–2–3–4 and it is predicted to be $\phi_{1234} = 128.1°$. The neighbored hexagonal and tetragonal rings are neither coplanar and its dihedral angle $\phi_{2345} = 140.6°$. Similarly, for the TH-SiC structure in Fig. 1(b), the corresponding geometry parameters are $a = 5.53$ Å, $b = 7.63$ Å, $d = 1.60$ Å, $r_1 = 1.88$ Å, $r_2 = 1.72$ Å, $\alpha = 116.1°$, $\beta = 118.9°$, $\gamma = 94.6°$, $\phi_{1234} = 126.8°$, $\phi_{2345} = 149.5°$. These parameters on the 2D TH-SiC structure are in great agreement with a recently reported work [29].

Table 1 gives a summary of some structural parameters and basic properties of the proposed 2D TH-SiC_2 and TH-SiC, along with penta-SiC_2 [28], tetrahex-carbon [22,43], penta-graphene [17], graphene and low-buckled silicene [7,27]. Comparing the buckling thickness and two typical bond lengths in TH-SiC_2 with those in penta-SiC_2, their values are close. While for TH-SiC, the bond r_2 is significantly lengthened since it describes Si—C bonds in TH-SiC instead of C—C bonds as in TH-SiC_2. The buckling thickness d is also increased indicating the structure of TH-SiC is more buckled compared to TH-SiC_2 and penta-SiC_2.

Cohesive energy E_{coh} for a general silicon carbide compound Si_xC_y is computed using the following equation,

$$E_{coh} = \frac{E_{tot}(Si_xC_y) - xE_{Si} - yE_C}{x + y}, \tag{1}$$

where E_{tot}, E_{Si}, E_C are the total energy of the material, and the energies of an isolated silicon and carbon atoms, respectively. The formation energy E_{form} per atom can then be obtained as follows [44,45],

$$\begin{aligned} E_{form} &= E_{coh}(Si_xC_y) - \frac{x}{x+y}\mu_{Si} - \frac{y}{x+y}\mu_C, \text{ or} E_{form} \\ &= \frac{E_{tot}(Si_xC_y) - x\,E(Si) - y\,E(C)}{x+y}, \end{aligned} \tag{2}$$

where μ_{Si}, μ_C, are cohesive energy per atom in silicene and graphene, respectively, $E(Si)$, $E(C)$ are the total energies per atom in

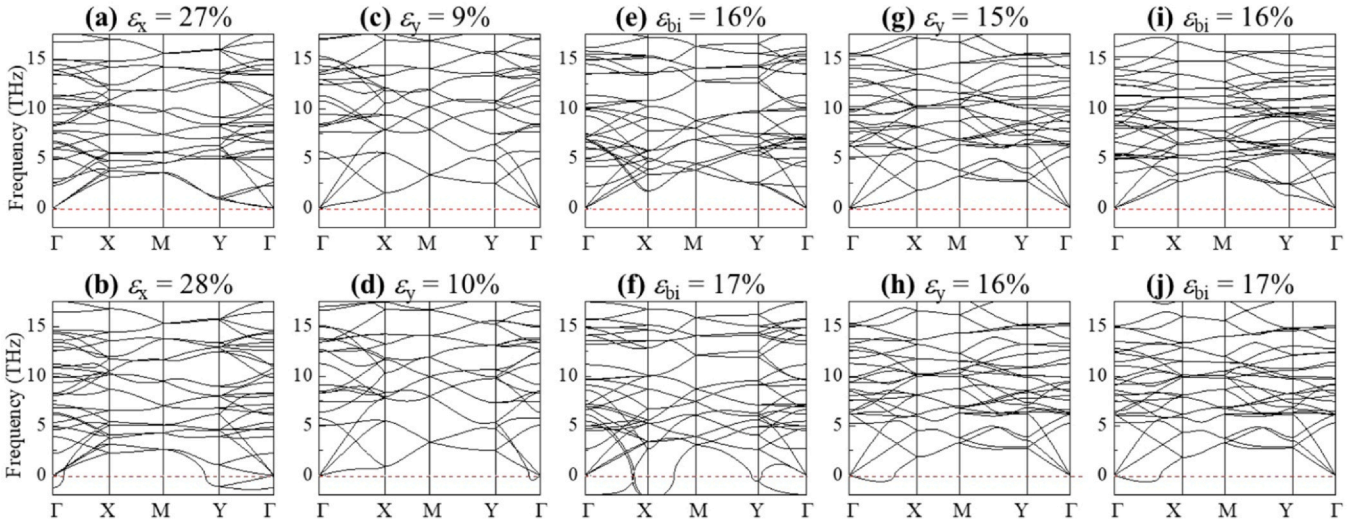

Fig. 3. Phonon spectra in the strained 2D (a)–(f) TH-SiC_2 and (g)–(j) TH-SiC nanostructures. The appearance of negative frequencies at the bottom row indicates structural instability. The notations $\varepsilon_x/\varepsilon_y$, and ε_{bi} on the top of figures represent uniaxial strain in the zigzag/armchair direction and biaxial strain, respectively.

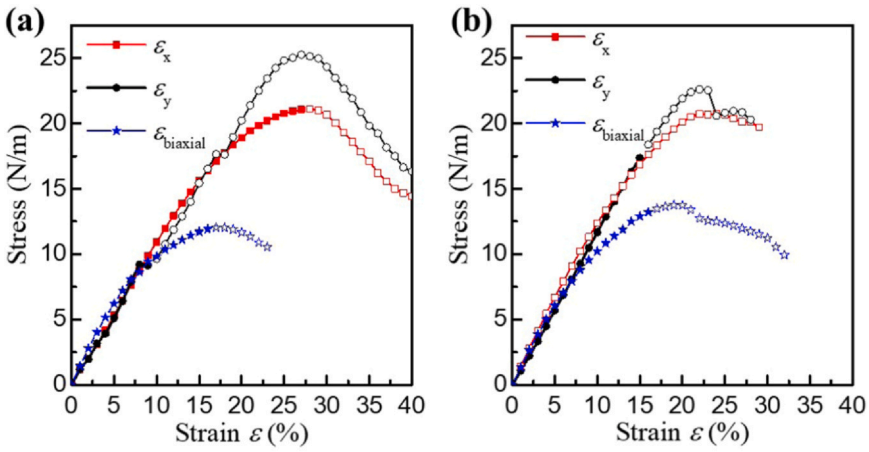

Fig. 4. The strain-stress relation in the 2D (a) TH-SiC_2 and (b) TH-SiC for uniaxial strain applied in the zigzag (x), armchair (y), and biaxial directions, respectively. Phonon instability occurs for TH-SiC_2 when strain is beyond 27%, 9%, and 16% in the x, y, and biaxial directions with the corresponding strength 21.1, 9.1, and 11.9 N/m, respectively. For TH-SiC, phonon instability occurs when strain is beyond 15% in the y axis and 16% biaxial strain with corresponding strength 17.4 and 13.2 N/m, respectively. TH-SiC is found not stable at all for uniaxial strain applied in the zigzag direction. Solid and hollow symbols represent phonon stable and instable, respectively.

silicene and graphene, respectively. Note that $\mu_{Si} = E(Si) - E_{Si}$ and $\mu_C = E(C) - E_C$.

The calculated cohesive and formation energies are provided in Table 1. Fig. 1(c) plots their cohesive energy along with some other 2D Si_xC_{1-x} compounds. The green dashed line connecting the energies of graphene and silicene is used to gauge the formation energy. The formation energy is positive (negative) above (below) the line. For structural details, one can refer to pertinent papers: para SiC_3 [25], penta-SiC_2 [28], g-SiC [42], g-SiC_2 [24], pt-SiC_2 [23], t-SiC [27], t-Si_2C [27].

It is found that in Fig. 1(c) TH-SiC_2 has a lower cohesive energy by 0.17 eV/atom compared to that of the planar pt-SiC_2 [23]. It has slightly higher cohesive energy by 0.04 eV/atom, compared to penta-SiC_2. This is opposite to their carbon counterparts since tetrahex-C is slightly energetically more favorable than penta-graphene (i.e. −7.12 versus −7.09 eV/atom). The formation energy of TH-SiC_2 is found to be 0.44 eV/atom, which is 0.04 eV/atom higher than that of penta-SiC_2. On the other hand, TH-SiC has a lower cohesive energy by 0.06 eV/atom compared to that of t-SiC [27], while a higher energy by 0.38 eV/atom to that of g-SiC [42]. The positive formation energy in TH-SiC_2 and TH-SiC indicates that their structures are metastable, similar to many other Si_xC_{1-x} compounds as presented in Fig. 1(c).

The 2D TH-SiC_2 and TH-SiC structures are proven to be thermodynamically stable according to the phonon spectrum calculations as shown in Fig. 2. No imaginary frequencies are found in the phonon spectra for the structures, indicating that they are stable. The stability of the structures under mechanical strain are also explored. Starting with the fully relaxed 2D crystal structures of TH-SiC_2 and TH-SiC, biaxial and uniaxial tensile strain up to 40% at an increment of 1% is applied in either the *x* (**a** or zigzag) or *y* (**b** or armchair) direction. The tensile strain is defined as,

$$\varepsilon = \frac{a - a_0}{a_0} \quad (3)$$

where *a* and a_0 are the lattice constants of the strained and relaxed structures, respectively. In the case of uniaxial strain applied in one direction, the lattice constant in the transvers direction is fully relaxed to ensure minimal stress in the transverse direction.

The phonon spectra of the materials under various values of strain are shown in Fig. 3. No negative frequency is observed in the top row of the spectra. However, negative frequencies appear in the bottom row, indicating instability of the structures. TH-SiC_2 structure remains stable up to 27%, 9% and 16% for the uniaxial strains in the zigzag, armchair directions, and biaxial strain, respectively. While TH-SiC is stable up to 15% and 16% for the uniaxial strain in the armchair direction and biaxial strain, respectively. Higher strain than those values bring in negative frequencies in the spectra and suggest that the structures are no longer stable. Interestingly, TH-SiC is unstable for any value of strain applied in the *x*-direction.

3.2. Mechanical properties and mechanical stability

The mechanical properties and stability of the new structures are also studied thoroughly. The study of strain-stress relation in a material can determine its ideal strength (the highest strength of a crystal at 0 K) [46,47] and critical strain (at which ideal strength reaches) [48]. To obtain the strain-stress relation in the 2D TH-SiC_2 and TH-SiC structures, uniaxial tensile strain along both *x* (zigzag), *y* (armchair) directions and biaxial strain are applied to the materials with an increment of 1% up to 40%. The results are given in Fig. 4. The strain-stress relation is calculated using the method described in the references [49,50], which was designed for three dimensional (3D) material. For a 2D system, the stress calculated from the DFT calculations has to be adjusted since DFT reported stress is largely underestimated due to averaging force over vacuum space. To avoid this effect, the stress in this work adopts the force per unit length in the unit of N/m. It is found that TH-SiC_2 and TH-SiC are more ductile in the *x* (zigzag) direction, similar to the case of tetrahex-C [43].

As mentioned previously, phonon instability occurs in TH-SiC_2 when strain is beyond 27%, 9%, and 16% in the *x*, *y*, and biaxial directions, respectively. Solid symbols in Fig. 4 represent stable structures and hollow symbols for unstable structures.

Table 2
A summary of mechanical parameters in TH-SiC_2 and TH-SiC. The elastic stiffness constants C_{ij}, Young's moduli E along the x and y directions, and the shear modulus G_{xy} are in unit of N/m.

Structures	C_{11}	C_{22}	C_{33}	C_{12}	E_x	E_y	G_{xy}	ν_{xy}	ν_{yx}
TH-SiC_2	119.7	123.3	57.3	26.5	114.0	117.4	57.3	0.22	0.22
TH-SiC	143.7	107.7	41.8	2.8	143.6	107.6	41.8	0.025	0.019

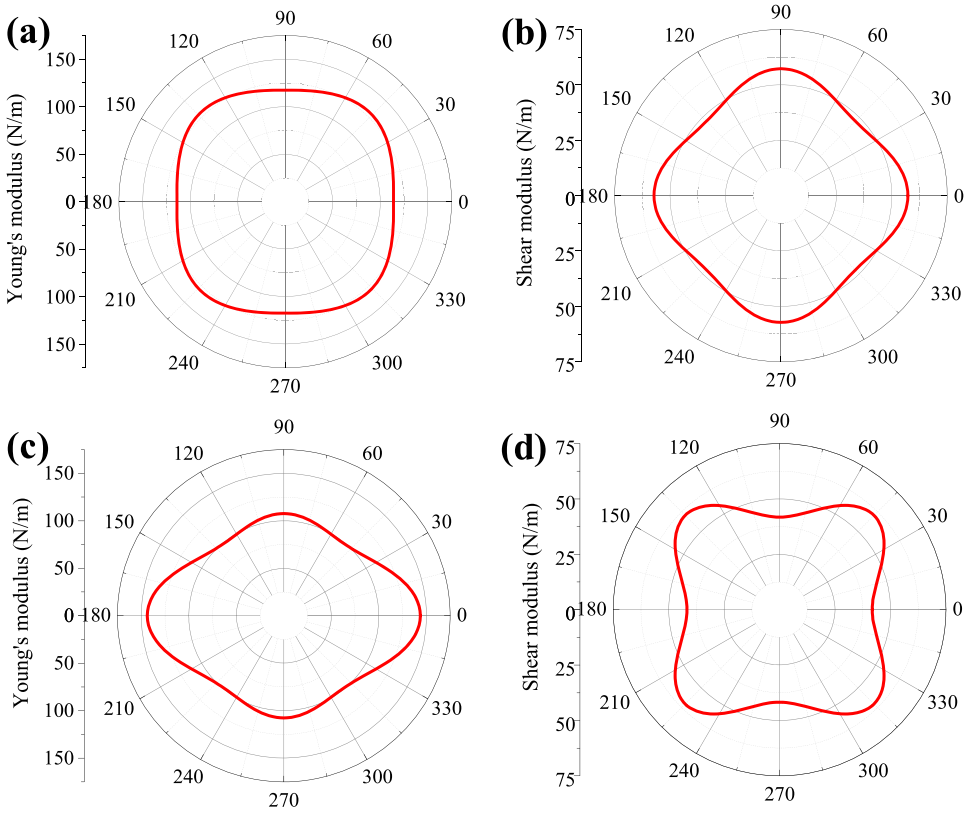

Fig. 5. The directional dependence of (a)(c) Young's modulus and (b)(d) shear modulus in the TH-SiC_2 (top) and TH-SiC (bottom).

Consequently, the ideal strength of TH-SiC_2 is found to be 21.1, 9.1 and 11.9 N/m in the *x*, *y* and biaxial direction, respectively. This high strength of 21.1 N/m is close to that in penta-graphene (23.5 N/m strength with 18% uniaxial strain in both zigzag and armchair directions) [51]. However, it is lower than that of graphene [47] and tetrahex-C [43]. On the other hand in TH-SiC, phonon instability occurs when strain is beyond 15% in the *y* axis and 16% biaxial strain with corresponding strength 17.4 and 13.2 N/m, respectively. This structure is found not stable at all for any uniaxial strain applied in the zigzag direction. Our reported strength values in TH-SiC are smaller than those in the reference [29], since the referenced work does not consider phonon stability for the strained structure. Its reported ultimate tensile strength values 25, 23 and 21 N/m for *x*, *y*, and biaxial strains, respectively, occur at the strains which we have proved that the phonon spectrum of the structure is no longer stable as shown in Fig. 3.

The energy surfaces of the 2D TH-SiC_2 and TH-SiC structures are scanned in the small strain range $-0.6\% < \varepsilon_{xx} < +0.6\%$, $-0.6\% < \varepsilon_{yy} < +0.6\%$, and $-0.6\% < \varepsilon_{xy} < +0.6\%$ to calculate their elastic stiffness constants and various moduli. The strain energy is defined as the energy difference between the strained and relaxed structures,

$$E_s = E(\varepsilon) - E_0 \tag{4}$$

where $E(\varepsilon)$andE_0 are the total energy of strained and relaxed structures, respectively. The calculated strain energy is then fitted parabolically using the following equation, to determine the coefficients a_i, and the elastic stiffness constants are readily calculated as,

$$E_s = a_1\varepsilon_{xx}^2 + a_2\varepsilon_{yy}^2 + a_3\varepsilon_{xx}\varepsilon_{yy} + a_4\varepsilon_{xy}^2 \tag{5}$$

$$C_{ij} = \frac{1}{A_0}\left(\frac{\partial E_s^2}{\partial\varepsilon_i\varepsilon_j}\right), \tag{6}$$

where $i, j = xx, yy$, or xy, A_0 is the area of the simulation cell in the *xy* plane. The Young's and shear moduli for a 2D system can be derived as a function of a_i [43,48],

$$E_x = \frac{4a_1a_2 - a_3^2}{2a_2A_0},\ E_y = \frac{4a_1a_2 - a_3^2}{2a_1A_0},\ G_{xy} = \frac{2a_4}{A_0}. \tag{7}$$

When uniaxial strain is applied in one direction, the lattice constant in the transverse direction needs to be fully relaxed to ensure minimal stress in the transverse direction. And the response strain in the transverse direction can be also calculated according to Eq. (3). Poisson's ratio can then being readily calculated according to its definition,

$$v = -\frac{\varepsilon_{transverse}}{\varepsilon_{axial}},\quad v_{xy} = -\frac{\varepsilon_y}{\varepsilon_x},\quad v_{yx} = -\frac{\varepsilon_x}{\varepsilon_y} \tag{8}$$

where $\varepsilon_{axial}$and$\varepsilon_{transverse}$ are the applied axial strain and its response strain in the transverse direction, respectively.

The calculated mechanical parameters in TH-SiC_2 and TH-SiC are listed in Table 2. The Poisson's ratios in TH-SiC is significantly smaller than those in TH-SiC_2 due to its smaller value of C_{12}. The elastic constants can be used to check the mechanical stability of the structures. The positive values in the elastic matrix in TH-SiC2 and TH-SiC (see Table 2) suggest the mechanical stability of these new structures. Our predicted parameters for TH-SiC are in great consistence with a recently reported work [29].

Young's and shear moduli along an arbitrary direction can be calculated using the methods described in [48] with the angle of an arbitrary direction from the + *x* axis. The direction dependence of the Young's and shear moduli in TH-SiC_2 and TH-SiC are presented in Fig. 5. For TH-SiC_2, the maximal Young's modulus is along the [11] direction (i.e. 45° from the *x* axis) with a value of 129 N/m, while a minimum of 114 N/m is along the *x* axis as shown in Fig. 5(a). However, it is opposite for TH-SiC. The Young's modulus has the minimum value of 99 N/m along the [11] direction while the largest

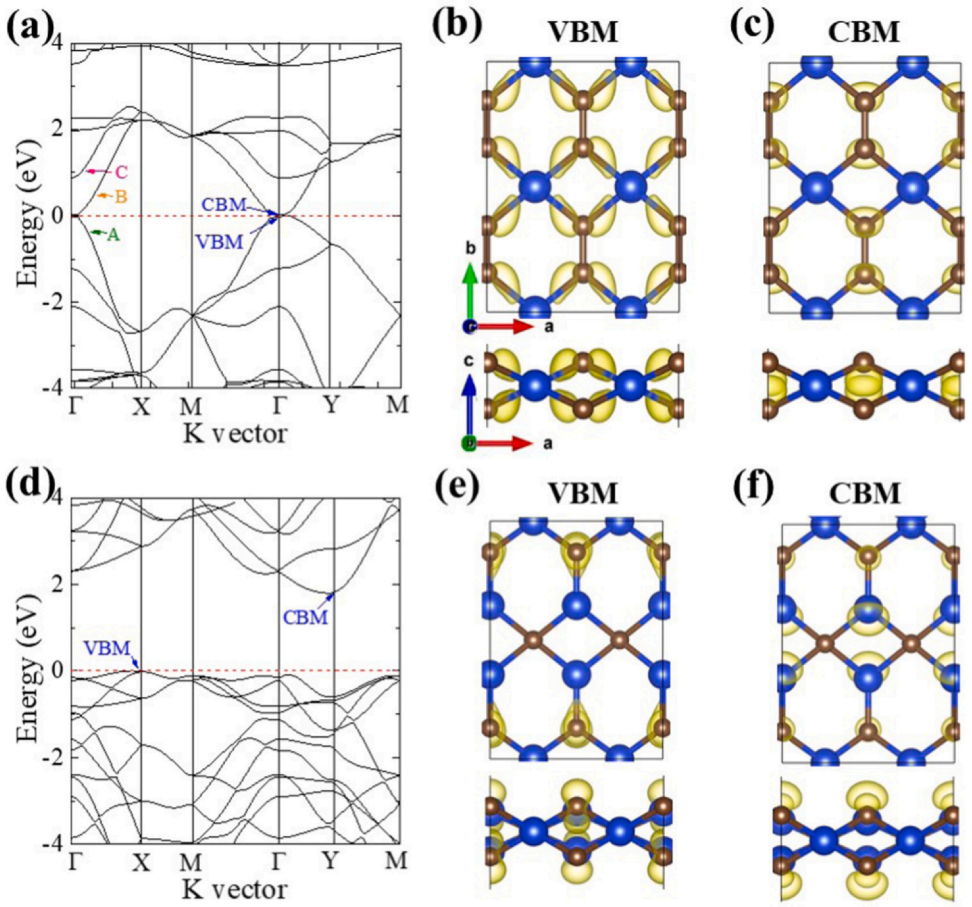

Fig. 6. (a) The HSE predicted electronic band structure of the relaxed TH-SiC_2 and the electron density contour plots of (b) VBM and (c) CBM, respectively. (d)-(f) The band structure and VBM/CBM plots for TH-SiC. The energy of VBM is set at zero. Si and C atoms are in blue and brown, respectively. The isosurface value for the electron density is set at 0.01 e/$Bohr^3$ (For interpretation of the references to colour in this figure legend, the reader is referred to the web version of this article.).

value of 144 N/m in the *x* direction as shown in Fig. 5(c). In the case of shear strain displayed in Fig. 5(b) (d), TH-SiC_2 has the maximal shear modulus of 57 N/m in the *x* and *y* directions, and a minimum value of 47 N/m along the [11] direction. However, for TH-SiC, the minimum 42 N/m occurs in the *x* and *y* directions while the maximum 60 N/m along the [11] direction. Fig. 5 demonstrates a strong anisotropicity in the 2D TH-SiC_2 and TH-SiC structures.

3.3. Electronic properties

Electronic band structures of the 2D TH-SiC_2 and TH-SiC are presented in Fig. 6(a) and (d) using the hybrid HSE06 functional. It shows that TH-SiC_2 possesses a direct band gap with a tiny value of 0.02 eV while TH-SiC has an indirect band gap with a value of 1.80 eV. Note that the standard PBE functional predicts no gap for TH-SiC_2 due to its well-known effect of underestimating band gap of semiconductors. No gap in TH-SiC_2 was also validated by two more density functionals PBEsol [52] and DFT-D3 [53]. The hybrid HSE06 functional has an improved accuracy on predicting band gaps and it suggests a tiny gap of 0.02 eV for TH-SiC_2. The valence band maximum (VBM) and conduction band minimum (CBM) in TH-SiC_2 are located at Γ. However, for the TH-SiC structure, VBM is located at X while CBM is at Y.

The electron density contour plots of VBM/CBM in both structures are also presented in Fig. 6. Through an analysis of the *spd*-orbital site projections of the VBM and CBM, it is found that the VBM in TH-SiC_2 is dominantly contributed by the p_x orbitals on all 12 atoms (4 Si and 8 C) in the conventional cells as shown in Fig. 6(b). However, the CBM is dominated by the p_z orbitals mainly located on the sp^2-hybridized C atoms as shown in Fig. 6(c). On the other hand for the TH-SiC structure, the electron charge of the VBM is dominantly contributed by the p_z orbitals on the sp^2 C atoms as shown in Fig. 6(e), while the CBM is located on both C and Si atoms as displayed in Fig. 6(f).

The tiny band gap of 0.02 eV in TH-SiC_2 can be opened up through various strategies. Here, we present two different means to manipulate its band gap. The first method is through hydrogenation by adsorbing hydrogen atoms on either or both sides of the nanosheet. The results are presented in Fig. 7. It can been seen that hydrogen adsorbed on either or both sides of the nanosheet can open up the band gap significantly in TH-SiC_2. In the case of single-side hydrogenation, the band gap is predicted to be 0.89 eV by the HSE functional with both VBM and CBM located at Γ as shown in Fig. 7(a). For the both sides of H adsorption, the band gap becomes indirect with a gap value of 1.72 eV. The VBM is still located at Γ. However, the CBM shifts from Γ to Y as shown in Fig. 7(e). Fig. 7 also provides the electron density contour plots of the VBM and CBM. It is found that in both cases, VBM shows similar charge distribution in Fig. 7(c) and (g) as in Fig. 6(b), where the state is mainly contributed by the p_x orbitals located on all Si/C atoms in the conventional cell. However, it is distinct in CBM. For half-H passivation, the CBM in Fig. 7(d) is dominated by the p_z orbitals located on the sp^2-C atoms. However, for the full-H passivation, the CBM in Fig. 7(h) is primarily contributed by the *s-p* hybridization of the C-H bonds.

Comparing the band structures in Fig. 6(a) for the pristine TH-SiC_2, and Fig. 7(a) and 7(e) with H adsorption, it can reveal the

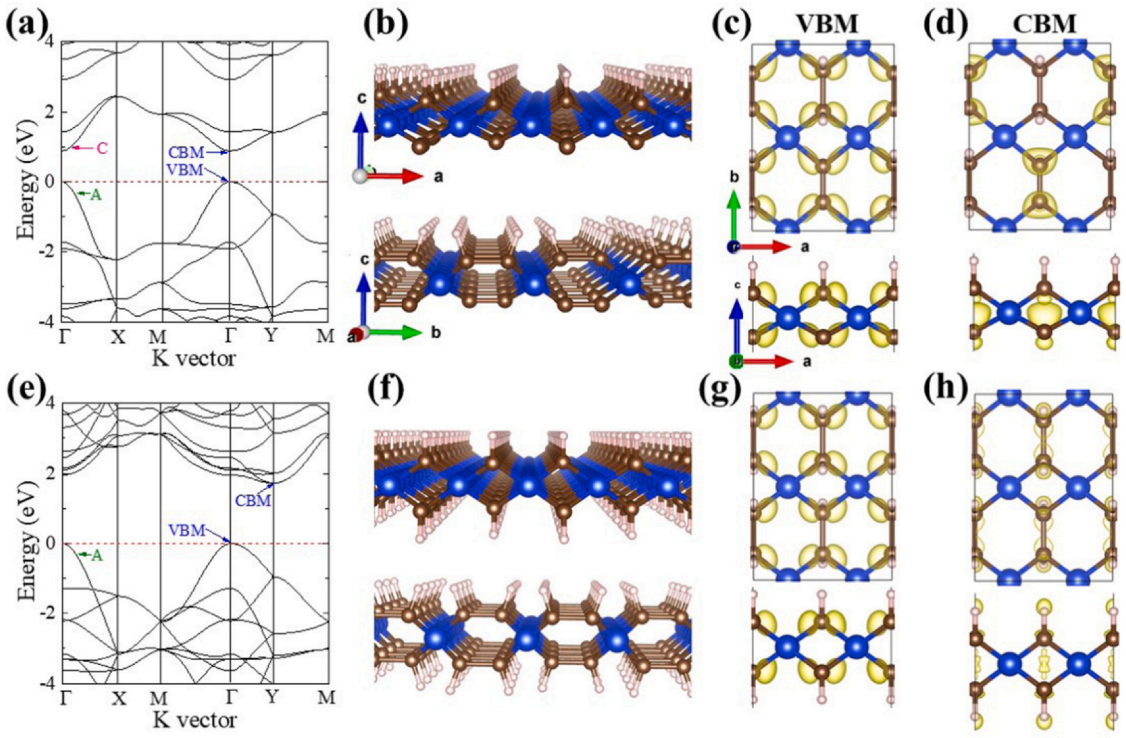

Fig. 7. Band gap opening through hydrogenation of TH-SiC_2. (a)–(d) H adsorbed on one side of the nanosheet, (e)–(h) H adsorbed on both sides of the nanosheet. (a)(e) HSE predicted band structures, (b)(f) schematics of hydrogenation, electron density contour plots of (c)(g) VBM and (d)(h) CBM. Si, C, H atoms are in blue, brown, and grey, respectively.

mechanism for band gap opening through hydrogenation. As shown in Fig. 6(a), the lowest and second lowest conduction bands are labeled as bands B and C, respectively. The electron charge of the band B (i.e. CBM) is primarily contributed by the p_z orbitals located on the sp^2-hybridized C atoms as shown in Fig. 6(c). Hydrogen adsorption on the structure converts these sp^2 C atoms into sp^3 hybridization. This removes the band B and leads to the band structure as shown in Fig. 7(a). The second lowest band C is also dominated by the p_z orbitals located on the sp^2-C atoms as displayed in Fig. 7(d). Full hydrogen absorption on both sides of the nanosheet completely passivates all sp^2-C atoms and converts them into sp^3-C, therefore, band C also disappears in Fig. 7(e). On the other hand for the valence band, the band A (i.e. VBM) is mainly contributed by the p_x orbitals located at all Si/C atoms including the middle sublayer of sp^3-Si atoms. Consequently, this band is not removed through hydrogenation.

The second method to open up the band gap in TH-SiC_2 is applying mechanical strain. Figs. 8 and 9 present the strain effects on the electronic properties in TH-SiC_2 and TH-SiC, respectively. Fig. 8(a) shows the band structure variation with strain in TH-SiC_2. The uniaxial strain is applied in the zigzag (x) direction. It is found that strain opens the band gap and maintains the nature of direct gap in the strain range up to 27% till phonon instability occurs. Biaxial and uniaxial strain in the y axis are not able open the band gap. Fig. 8(b) presents the gap variation with the uniaxial strain. The energy variation of the VBM and CBM is given in Fig. 8(c), in which the CBM energy increases while VBM reduces within the strain range till 12%. These different energy variation trends are related to their specific orbitals shape and bonding/antibonding nature in the x direction. From the charge distribution of the VBM and CBM shown in Fig. 8(d) and (e), one can conclude that VBM exhibits antibonding characteristics along the x direction while CBM demonstrates bonding nature. With axial strain applied in the x direction, the energy variation with strain of the state obeys a pattern schematically illustrated in Fig. 8(f) [54,55]. This schematics is obtained from the exchange energy model suggested by Heitler-London [56], in which the energies of the bonding and antibonding states are distinct in terms of the exchange-correlation energy of electrons. The exchange-correlation energy is resulted from either non-classical electron-electron (positive) or electron-ion interaction (negative) with the latter dominant for orbitals with a non-localized electron density. Consequently, tensile strain increases bond lengths and the energy of bonding states increases while that of anti-bonding states reduces [54,55]. The energy variation of VBM and CBM in Fig. 8(c) is beautifully explained by this model.

Similarly, the band structure and gap in TH-SiC can also be effectively manipulated via strain as shown in Fig. 9. Since this structure is not stable with uniaxial strain applied in the x-axis, we only report the results of biaxial and axial strains in the y axis. For the uniaxial strain in the y direction as demonstrated in Fig. 9(a), it is found that the band gap remains indirect. However, both CBM and VBM shift to different K vectors. Without strain, the VBM and CBM in TH-SiC are located at X and Y, respectively. With the application of 12% uniaxial strain in the y direction (dashed lines in Fig. 9(a)), the VBM moves away from X toward a K-vector along Γ-X, and CBM shifts from Y toward Γ. A similar story occurs for the biaxial strain as shown in Fig. 9(b), where the VBM locates nearby the K-vector of M and CBM is in the middle point along Γ-Y. The band gap variation with strain is presented in Fig. 9(c). All of the calculated band gaps are indirect and there is no indirect-direct band gap transition observed. Fig. 9(c) also suggests that the biaxial strain is more effective to tune the band gap compared to the uniaxial strain.

4. Summary

Employing first-principles DFT calculations, we propose a set of new 2D silicon carbide nanostructures. We find the nanosheets are thermodynamically and mechanically stable. The relatively low cohesive and formation energies suggest a possibility of experimental synthesis of the materials. The new structures exhibit strong

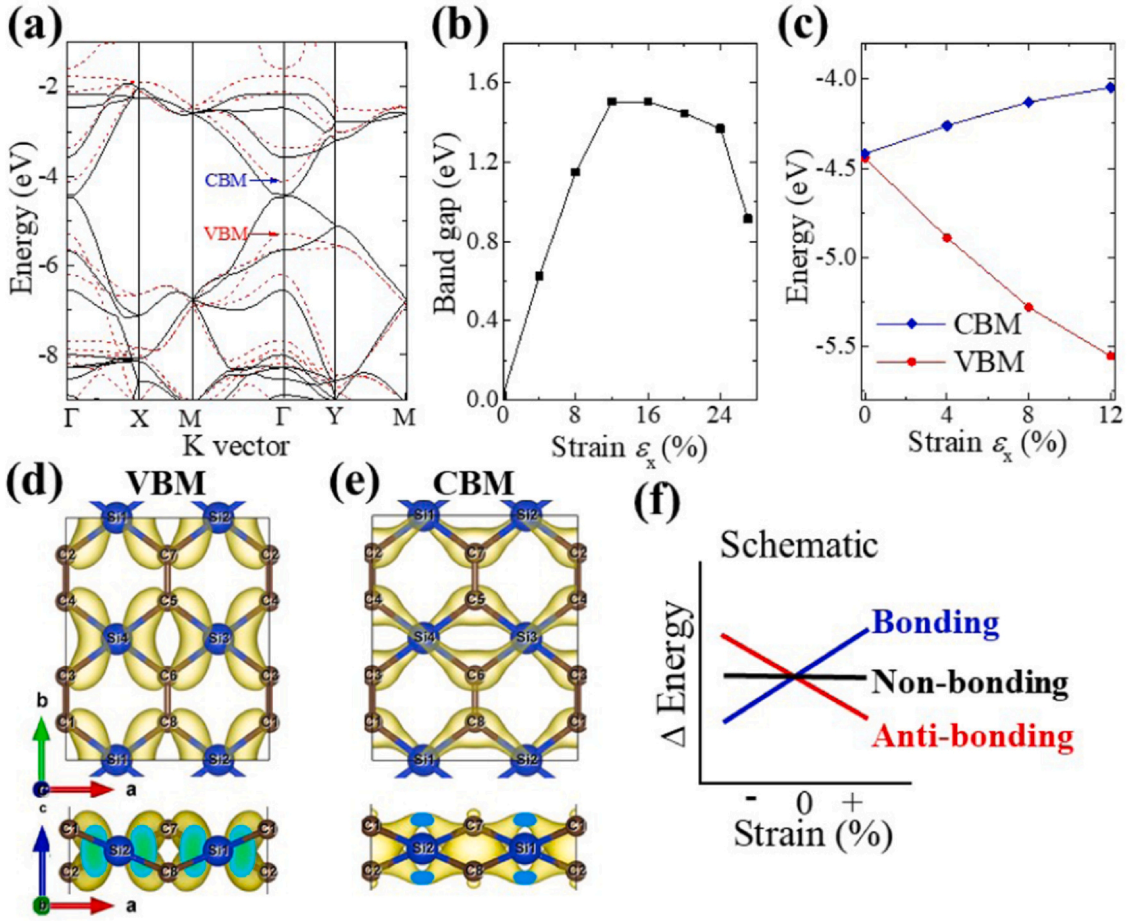

Fig. 8. Band gap opening through strain application in TH-SiC_2. (a) The HSE band structure without strain (solid lines) and with 8% uniaxial strain applied in the zigzag direction (dashed lines), (b) band gap as a function of uniaxial strain, (c) energy variation of the VBM and CBM with strain, respectively. All band gaps in (b) are direct gap. Energies are reference to vacuum level. Electron density contour plots of (d) VBM and (e) CBM at the isosurface value of 0.004 e/$Bohr^3$. (f) A schematic of energy response to axial strain for three typical cases of bonding, non-bonding, and anti-bonding.

anisotropicity though the exploration of the strain-stress relation and the directional dependency of mechanical moduli with superior ductility. TH-SiC_2 structure has a tiny direct band gap with a value of 0.02 eV predicted by the HSE06 functional. However, the band gap can readily open up through various strategies including hydrogenation and strain application. The gap values can be tuned in the range of 0.02–1.72 eV, and the gap nature of direct/indirect can be manipulated. On the other hand, the 2D TH-SiC structure demonstrates an indirect HSE band gap of 1.80 eV and strain is found to be effectively tune the gap between 0.0–1.95 eV. The ductility, anisotropicity, tunable band gap and direct/indirect gap nature in these 2D TH-SiC_2 and TH-SiC may have potential applications in nanomechanics and nanoelectronics.

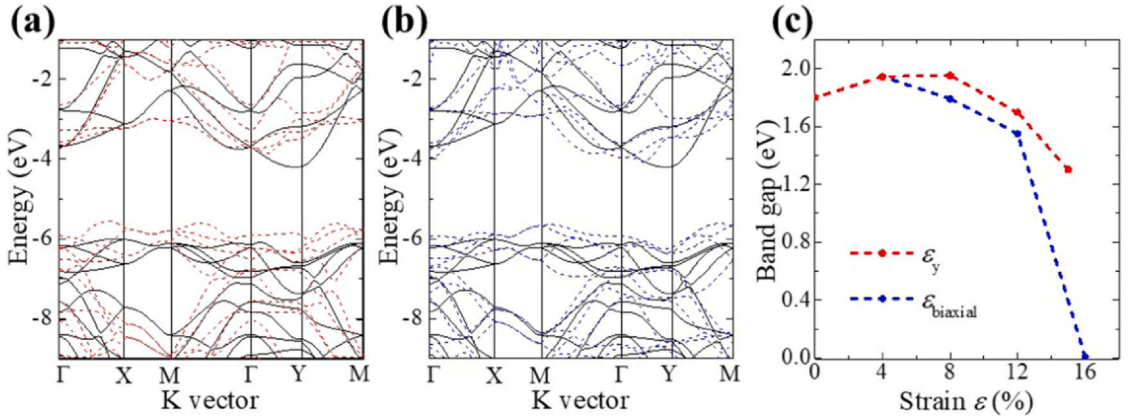

Fig. 9. Band structure and gap variation with strain in the 2D TH-SiC nanosheet. The HSE band structure without strain (solid lines) and with (a) 12% uniaxial strain in the armchair direction (dashed lines), (b) 12% biaxial strain (dashed lines). Energy is referenced to vacuum level. (c) The HSE band gap in the 2D TH-SiC as a function of strain and all gaps are indirect within the range with phonon stability.

CRediT authorship contribution statement

Qun Wei: Methodology, Software, Writing - reviewing and editing, Resources. **Ying Yang:** Methodology, Software, Visualization. **Guang Yang:** Methodology, Software, Investigation. **Xihong Peng:** Methodology, Conceptualization, Visualization, Supervision, Validation, Resources, Writing - original draft preparation, Data curation.

Declaration of Competing Interest

The authors declare that they have no known competing financial interests or personal relationships that could have appeared to influence the work reported in this paper.

Acknowledgement

This work is financially supported by the Fundamental Research Funds for the Central Universities, the Natural Science Foundation of China (Grant No.: 11965005), the 111 Project (B17035), and the Natural Science Basic Research plan in Shaanxi Province of China (Grant No.: 2020JM-186). The authors thank Arizona State University Advanced Computing Center for providing computing resources (Agave Cluster), and the computing facilities at High Performance Computing Center of Xidian University.

References

[1] K.S. Novoselov, A.K. Geim, S.V. Morozov, D. Jiang, Y. Zhang, S.V. Dubonos, I.V. Grigorieva, A.A. Firsov, Electric field in atomically thin carbon films, Science 306 (2004) 666–669.
[2] K.S. Novoselov, A.K. Geim, S.V. Morozov, D. Jiang, M.I. Katsnelson, I.V. Grigorieva, S.V. Dubonos, A.A. Firsov, Two-dimensional gas of massless Dirac fermions in graphene, Nature 438 (2005) 197–200.
[3] J.C. Meyer, A.K. Geim, M.I. Katsnelson, K.S. Novoselov, T.J. Booth, S. Roth, The structure of suspended graphene sheets, Nature 446 (2007) 60–63.
[4] P. Vogt, P. De Padova, C. Quaresima, J. Avila, E. Frantzeskakis, M.C. Asensio, A. Resta, B. Ealet, G. Le Lay, Silicene: compelling experimental evidence for graphenelike two-dimensional silicon, Phys. Rev. Lett. 108 (2012) 155501.
[5] A. Fleurence, R. Friedlein, T. Ozaki, H. Kawai, Y. Wang, Y. Yamada-Takamura, Experimental evidence for epitaxial silicene on diboride thin films, Phys. Rev. Lett. 108 (2012) 245501.
[6] B. Feng, Z. Ding, S. Meng, Y. Yao, X. He, P. Cheng, L. Chen, K. Wu, Evidence of silicene in honeycomb structures of silicon on Ag(111), Nano Lett. 12 (2012) 3507–3511.
[7] S. Cahangirov, M. Topsakal, E. Aktürk, H. Šahin, S. Ciraci, Two- and one-dimensional honeycomb structures of silicon and germanium, Phys. Rev. Lett. 102 (2009) 236804.
[8] K. Nakada, M. Fujita, G. Dresselhaus, M.S. Dresselhaus, Edge state in graphene ribbons: nanometer size effect and edge shape dependence, Phys. Rev. B 54 (1996) 17954–17961.
[9] P. De Padova, P. Perfetti, B. Olivieri, C. Quaresima, C. Ottaviani, G. Le Lay, P. De Padova, P. Perfetti, B. Olivieri, C. Quaresima, C. Ottaviani, G. Le Lay, 1D graphene-like silicon systems: silicene nano-ribbons, J. Phys. Condens. Matter 24 (2012) 223001.
[10] H.J. Xiang, B. Huang, Z.Y. Li, S.-H. Wei, J.L. Yang, X.G. Gong, Ordered semiconducting nitrogen-graphene alloys, Phys. Rev. X 2 (2012) 011003.
[11] K.F. Mak, C.H. Lui, J. Shan, T.F. Heinz, Observation of an electric-field-induced band gap in bilayer graphene by infrared spectroscopy, Phys. Rev. Lett. 102 (2009) 256405.
[12] M.H.F. Sluiter, Y. Kawazoe, Cluster expansion method for adsorption: application to hydrogen chemisorption on graphene, Phys. Rev. B. 68 (2003) 085410.
[13] E. Bekyarova, M.E. Itkis, P. Ramesh, C. Berger, M. Sprinkle, W.A. de Heer, R.C. Haddon, Chemical modification of epitaxial graphene: spontaneous grafting of aryl groups, J. Am. Chem. Soc. 131 (2009) 1336–1337.
[14] H. Liu, Y. Liu, D. Zhu, Chemical doping of graphene, J. Mater. Chem. 21 (2011) 3335–3345.
[15] F. Banhart, J. Kotakoski, A.V. Krasheninnikov, Structural defects in graphene, ACS Nano 5 (2011) 26–41.
[16] C. Si, Z. Sun, F. Liu, Strain engineering of graphene: a review, Nanoscale 8 (2016) 3207–3217.
[17] S. Zhang, J. Zhou, Q. Wang, X. Chen, Y. Kawazoe, P. Jena, Penta-graphene: a new carbon allotrope, Proc. Natl. Acad. Sci. 112 (2015) 2372–2377.
[18] Y. Liu, G. Wang, Q. Huang, L. Guo, X. Chen, Structural and electronic properties of T graphene: a two-dimensional carbon allotrope with tetrarings, Phys. Rev. Lett. 108 (2012) 225505.
[19] L.C. Xu, R.Z. Wang, M.S. Miao, X.L. Wei, Y.P. Chen, H. Yan, W.M. Lau, L.M. Liu, Y.M. Ma, Two dimensional Dirac carbon allotropes from graphene, Nanoscale 6 (2014) 1113–1118.
[20] M. Zhao, W. Dong, A. Wang, Two-dimensional carbon topological insulators superior to graphene, Sci. Rep. 3 (2013) 3–8.
[21] D. Malko, C. Neiss, F. Viñes, A. Görling, Competition for graphene: graphynes with direction-dependent dirac cones, Phys. Rev. Lett. 108 (2012) 086804.
[22] B. Ram, H. Mizuseki, Tetrahexcarbon: a two-dimensional allotrope of carbon, Carbon 137 (2018) 266–273.
[23] Y. Li, F. Li, Z. Zhou, Z. Chen, SiC_2 silagraphene and its one-dimensional derivatives: where planar tetracoordinate silicon happens, J. Am. Chem. Soc. 133 (2011) 900–908.
[24] L.J. Zhou, Y.F. Zhang, L.M. Wu, SiC_2 siligraphene and nanotubes: novel donor materials in excitonic solar cells, Nano Lett. 13 (2013) 5431–5436.
[25] Y. Ding, Y. Wang, Geometric and electronic structures of two-dimensional SiC_3 compound, J. Phys. Chem. C 118 (2014) 4509–4515.
[26] P. Borlido, A.W. Huran, M.A.L. Marques, S. Botti, Novel two-dimensional silicon-carbon binaries by crystal structure prediction, Phys. Chem. Chem. Phys. 22 (2020) 8442–8449.
[27] D. Fan, S. Lu, Y. Guo, X. Hu, Novel bonding patterns and optoelectronic properties of the two-dimensional SixCy monolayers, J. Mater. Chem. C 5 (2017) 3561–3567.
[28] Y. Z, H.Z. Y, Xu, Z. Ning, H. Zhang, G. Ni, H. Shao, B. Peng, X. Zhang, X. He, Anisotropic ultrahigh hole mobility in two-dimensional penta-SiC_2 by strain-engineering: electronic structure and chemical bonding analysis, RSC Adv. 7 (2017) 45705–45713.
[29] M.E. Kilic, K.-R. Lee, Tetrahex carbides: two-dimensional group-IV materials for nanoelectronics and photocatalytic water splitting, Carbon 174 (2020) 368–381.
[30] W. Kohn, L.J. Sham, Self-consistent equations including exchange and correlation effects, Phys. Rev. 140 (1965) A1133–A1138.
[31] J. Heyd, G.E. Scuseria, M. Ernzerhof, Hybrid functionals based on a screened Coulomb potential, J. Chem. Phys. 118 (2003) 8207–8215.
[32] J. Heyd, G.E. Scuseria, M. Ernzerhof, Erratum: "hybrid functionals based on a screened Coulomb potential", J. Chem. Phys. 124 (2006) 219906.
[33] G. Kresse, J. Furthmüller, Efficient iterative schemes for ab initio total-energy calculations using a plane-wave basis set, Phys. Rev. B 54 (1996) 11169–11186.
[34] G. Kresse, J. Furthmüller, Efficiency of ab-initio total energy calculations for metals and semiconductors using a plane-wave basis set, Comput. Mater. Sci. 6 (1996) 15–50.
[35] P.E. Blöchl, Projector augmented-wave method, Phys. Rev. B 50 (1994) 17953–17979.
[36] G. Kresse, D. Joubert, From ultrasoft pseudopotentials to the projector augmented-wave method, Phys. Rev. B 59 (1999) 1758–1775.
[37] J.P. Perdew, K. Burke, M. Ernzerhof, Generalized gradient approximation made simple, Phys. Rev. Lett. 77 (1996) 3865–3868.
[38] H.J. Monkhorst, J.D. Pack, Special points for Brillouin-zone integrations, Phys. Rev. B 13 (1976) 5188–5192.
[39] W.H. Press, B.P. Flannery, S.A. Teukolsky, W.T. Vetterling, Numerical recipes, Cambridge University Press, New York, 1986.
[40] A. Togo, I. Tanaka, First principles phonon calculations in materials science, Scr. Mater. 108 (2015) 1–5.
[41] K. Momma, F. Izumi, VESTA program, http://jp-minerals.org/vesta/en/. *Version 3* 2020.
[42] S.S. Lin, Light-emitting two-dimensional ultrathin silicon carbide, J. Phys. Chem. C 116 (2012) 3951–3955.
[43] Q. Wei, G. Yang, X. Peng, Auxetic tetrahex carbon with ultrahigh strength and a direct band gap, Phys. Rev. Appl. 13 (2020) 034065.
[44] Z. Shi, A. Kutana, B.I. Yakobson, How much N - doping can graphene sustain? J. Phys. Chem. Lett. 6 (2015) 106–112.
[45] Z. Zhang, X. Liu, B.I. Yakobson, W. Guo, Two-dimensional tetragonal TiC monolayer sheet and nanoribbons, J. Am. Chem. Soc. 134 (2012) 19326–19329.
[46] T. Li, J.W. Morris, N. Nagasako, S. Kuramoto, D.C. Chrzan, "Ideal" engineering alloys, Phys. Rev. Lett. 98 (2007) 105503.
[47] F. Liu, P. Ming, J. Li, Ab initio calculation of ideal strength and phonon instability of graphene under tension, Phys. Rev. B 76 (2007) 064120.
[48] Q. Wei, X. Peng, Superior mechanical flexibility of phosphorene and few-layer black phosphorus, Appl. Phys. Lett. 104 (2014) 251915.
[49] D. Roundy, M.L. Cohen, Ideal strength of diamond, Si, and Ge, Phys. Rev. B 64 (2001) 212103.
[50] W. Luo, D. Roundy, M.L. Cohen, J.W. Morris, Ideal strength of bcc molybdenum and niobium, Phys. Rev. B 66 (2002) 094110.
[51] H. Sun, S. Mukherjee, C.V. Singh, Mechanical properties of monolayer penta-graphene and phagraphene: a first-principles study, Phys. Chem. Chem. Phys. 18 (2016) 26736–26742.
[52] J.P. Perdew, A. Ruzsinszky, G.I. Csonka, O.A. Vydrov, G.E. Scuseria, L.A. Constantin, X. Zhou, K. Burke, Restoring the density-gradient expansion for exchange in solids and surfaces, Phys. Rev. Lett. 100 (2008) 136406.
[53] S. Grimme, J. Antony, S. Ehrlich, H. Krieg, A consistent and accurate ab initio parametrization of density functional dispersion correction (DFT-D) for the 94 elements H-Pu, J. Chem. Phys. 132 (2010) 154104.
[54] X. Peng, A. Copple, Origination of the direct-indirect band gap transition in strained wurtzite and zinc-blende GaAs nanowires: a first principles study, Phys. Rev. B 87 (2013) 115308.
[55] X. Peng, Q. Wei, A. Copple, Strain-engineered direct-indirect band gap transition and its mechanism in two-dimensional phosphorene, Phys. Rev. B 90 (2014) 085402.
[56] R.M. White, Quantum Theory of Magnetism, ed. 3rd., Springer, New York, 2006.